RSC Advances

ROYAL SOCIETY OF CHEMISTRY

PAPER

View Article Online
View Journal | View Issue

Cite this: *RSC Adv.*, 2026, **16**, 8441

Bio-inspired synthesis of Co-doped iron oxide nanoparticles using *Ocimum tenuiflorum* extract for enhanced oxygen evolution reaction

Mariam Khan, [a] Nadeem Raza, [b] Shamsa Munir, *[a] Faiza Asghar,[c] Salma Gul,[d] Shahid Afridi,[d] Nigarish Bano,[e] Mostafa E. Salem, [b] Anis Ahmad Chaudhary[f] and Zeeshan Ali *[g]

Meeting the energy demands of modern society remains a significant issue in pursuing safe, sustainable, and highly effective fuel generation. The oxygen evolution reaction (OER) is a contemporary method for hydrogen production and many novel electrocatalysts have been explored recently to enhance the efficiency of O_2 evolution. This study focuses on: (i) the green synthesis of iron oxide nanoparticles (NPs) using the leaf extract of *Ocimum tenuiflorum;* (ii) doping with transition/alkaline earth metals (Co, Zn, Mg, and Ca); and (iii) their OER potential. The NPs were characterized in detail *via* Fourier-transform infrared spectroscopy (FTIR), scanning electron microscopy (SEM), X-ray diffraction (XRD), UV-visible spectroscopy, and square wave voltammetry (SWV), all of which confirmed the successful formation of these NPs. A glassy carbon electrode modified with NPs was used to evaluate OER potential. The Co-doped NPs attained a high electrochemically active surface area (ECSA) of 0.089 cm^2, which also coincides with a high intrinsic activity attained *via* a Tafel slope of 58 mV dec^{-1} and turnover frequency (TOF) up to 0.38 s^{-1}. Among all variants, Co-doped nanoparticles exhibited superior electrocatalytic performance with the lowest E_{onset}, demonstrating their potential as an efficient and sustainable OER catalyst. This study underscores the potential of plant extract mediated approaches to synthesise NPs for application in energy conversion and storage devices.

Received 4th December 2025
Accepted 28th January 2026

DOI: 10.1039/d5ra09374k

rsc.li/rsc-advances

1. Introduction

The exhaustion of fossil fuels coupled with rising energy consumption, leading to a substantial energy crisis in the 21st century, has created great stress for the development of alternative sustainable and renewable energy resources.[1] Among several approaches, the oxygen evolution reaction (OER) has emerged as a promising route for hydrogen production through water splitting. Electrocatalytic water-splitting represents a viable approach for generating pure H_2 for commercial applications, as it operates at room temperature and is a scalable process that necessitates electrical energy. Currently, hydrogen represents a clean and sustainable energy source with high energy density and zero carbon emissions and is under extensive investigation for its potential to revolutionize the energy economy.[2,3]

Importantly, the success of water splitting is greatly dependent on OER kinetics which is sluggish and demands high energy inputs to overcome its four-electron transfer barrier. Therefore, the development of long-lasting, low-cost metal-based catalysts that can support anodic OER is exciting. The suitability of an electrocatalyst is evaluated through stability, high activity, numerous exposed active sites, and low electron transport barriers for efficient electrochemical water splitting (EWS) along with its fundamental physical properties including its structural phase transition.[4] To this end, changing the oxidation states, crystal topologies, and porous frameworks of some transition metals can greatly improve their catalytic activity.[5] Various benchmark catalysts such as RuO_2 and IrO_2 have been extensively employed to lower the overpotential required for water splitting however, their high cost, less durability, and scarcity make their monetary applications problematic.[6] Consequently, the main focus is shifted to explore the OER potential of abundant metal-based compounds/composites.

Recently, hematite (α-Fe_2O_3) has received substantial consideration owing to its tremendous attributes in terms of chemical stability in aqueous environments, an appropriate

[a]*Industrial Sciences Research Labs, NUTECH Research Center, National University of Technology, Islamabad-44000, Pakistan. E-mail: smunir@nutech.edu.pk*
[b]*Department of Chemistry, College of Science, Imam Mohammad Ibn Saud Islamic University (IMSIU), Riyadh, Saudi Arabia*
[c]*Department of Chemistry, Rawalpindi Women University, Rawalpindi, Pakistan*
[d]*National Centre of Excellence in Physical Chemistry, University of Peshawar, Peshawar, Pakistan*
[e]*Institute of Chemical Sciences, Bahauddin Zakariya University, Multan, Pakistan*
[f]*Department of Biology, College of Science, Imam Mohammad Ibn Saud Islamic University (IMSIU), Riyadh, Saudi Arabia*
[g]*Department of Climate Change, MNS-University of Agriculture Multan MNSUAM, Pakistan. E-mail: zeeshan.ali@mnsuam.edu.pk*

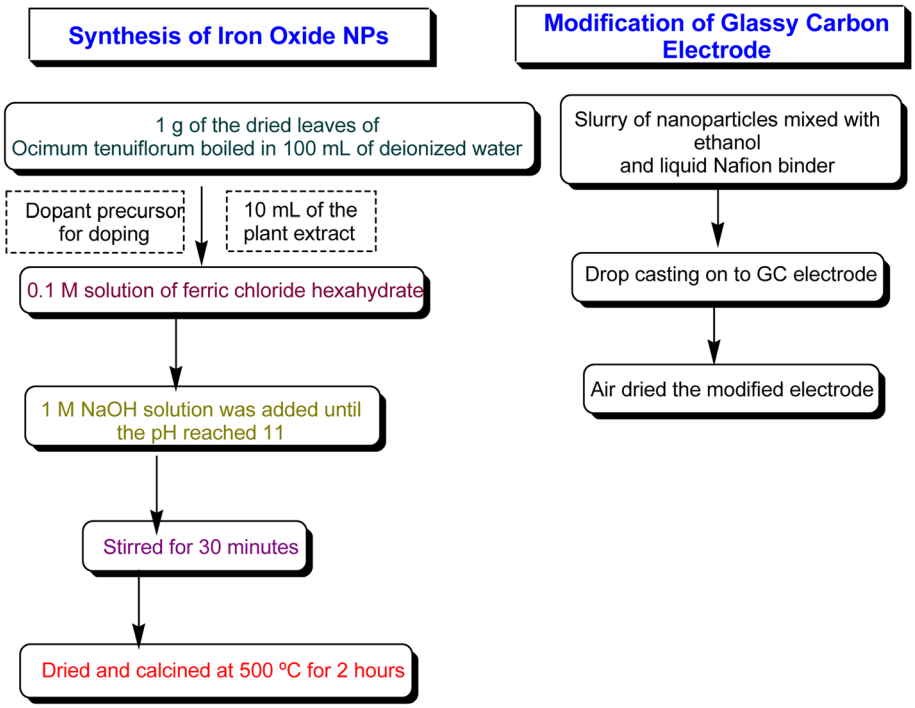

Scheme 1 Illustration for synthesis of iron oxide NPs and their modification on GCE.

energy band gap (1.9–2.2 eV) for light absorption, affordability, and eco-friendliness.[7] Hematite, due to its well-suited energy bandgap, can attain a theoretical maximum solar-to-hydrogen (STH) efficiency of 15%, above the projected STH benchmark efficiency of 10% for commercial applications.[8]

However, OER potential of pristine Fe_2O_3 is constrained *via* low charge-transportation, suboptimal electrical characteristics, and slow charge transfer resistance at interface of electrode/electrolyte.[9] To date, significant efforts have been devoted to enhancing the atomic and electronic structures of iron-based oxides through chemical component modification, the construction of nanostructures with dimensional confinement, the fabrication of low-crystallinity and amorphous catalysts, and doping with cations or anions. Specifically, doping of iron oxide with alkaline earth and transition metals (*i.e.*, Ca, Mg, Zn, and Co) has gained considerable attention due to modification in localized electronic structure leading to enhanced charge carrier density thus facilitating the conversion of oxygen intermediates during OER process.[10–14]

For example, Co and Zn doping have been shown to greatly increase the charge carrier mobility and OER kinetics of electrodes made of hematite.[15–18] Such modifications enable the researchers to design advanced electrocatalysts with superior activity and durability for OER applications. Generally, electrocatalysts are synthesized through conventional chemical and physical processes (incompatible with green chemistry concepts) which greatly rely on harsh environments and hazardous precursors. Therefore, more focus is to utilize bio-inspired greener approaches particularly through the deployment of plant extracts for the synthesis of electrocatalysts. Interestingly, diverse phytochemicals in plant extracts, including polyphenols, alkaloids, and flavonoids, serve as reducing agents for the synthesis of NPs with desirable morphologies and surface functionalities.[19]

The main aim of the current research was to fabricate an economically viable, efficient electrocatalyst with high OER potential by achieving low overpotential comparable to noble metals electrocatalysts with the aim of providing an enduring solution for water splitting catalysis. In the present study, we explored the synthesis of iron oxide, and their doped NPs utilizing a *Ocimum tenuiflorum* (commonly known as Holy Basil or Tulsi) leaf extract through a simple and greener approach to evaluate their potential for OER. Diverse instrumental techniques, including XRD, FTIR, SEM, UV-visible, and SWV, were employed to systematically analyze the pristine and doped iron oxide NPs. Electrochemical characteristics of pristine and doped NPs were evaluated by pasting them on glassy carbon electrodes (GCEs), and their OER performance was measured using linear scan and cyclic voltammetry (Scheme 1). This work underscores the potential of plant-mediated synthesis approach of cost-effective and scalable metal-doped iron oxide nanocatalysts for electrochemical and renewable energy benefits.

2. Experimental

2.1. Chemicals used

$FeCl_3 \cdot 6H_2O$ (Sigma-Aldrich, 98%), NaOH (Sigma-Aldrich, 98–100%), $CaCl_2 \cdot 2H_2O$ (Duksan, 97%), $MgCl_2 \cdot 6H_2O$ (Duksan, 98%), $ZnSO_4 \cdot 7H_2O$ (Duksan, extra pure grade), and $Co(No_3)_2 \cdot 6H_2O$ (Sigma-Aldrich, 98%) were utilized for the synthesis of NPs. Deionized water was used to prepare all solutions. The leaves of the *Osmium tenuiflorum* were taken from the local area of Wah Cantt, Pakistan.

2.2. Synthesis of iron oxide NPs

The leaf extract of *Ocimum tenuiflorum* was employed for green synthesis of iron oxide NPs. Fresh leaves of the plant were properly washed with water, dried, and then crushed. To prepare a concentrated extract, 1 g of dried leaves was boiled in 100 mL of deionized water. The resulting extract was kept in the refrigerator for future use.

For the synthesis of plant extract-based iron oxide NPs, a 0.1 M solution of ferric chloride hexahydrate ($FeCl_3 \cdot 6H_2O$) was prepared in deionized water. At room temperature, 10 mL of plant extract was added drop by drop into 10 mL of the 0.1 M $FeCl_3$ solution under alkaline conditions (pH = 11). The resultant mixture was agitated for 30 min to obtain dark brown iron oxide NPs which were washed thrice with deionized water, then dried in an oven at 60 °C for 1.5 h and calcined at 500 °C for 2 h. These iron oxide NPs are labelled as E-NPs in the forthcoming sections.

The same procedure was followed to synthesize Mg, Ca, Zn, and Co-doped iron oxide NPs, using 2% of the respective dopant precursor relative to the amount of $FeCl_3$ used to prepare 0.1 M $FeCl_3$ solution. The doped NPs synthesized using plant extract are labelled as E-M-NPs where M = Mg, Ca, Zn, and Co, in the forthcoming sections. Additionally, for comparison purposes, iron oxide NPs were synthesized without using the plant extract, following the above-mentioned procedure and are labeled as C-NPs.

2.3. Physical characterizations

All synthesized electrocatalysts were characterized by employing Fourier-transform infrared spectroscopy (FTIR), X-ray diffraction (XRD), scanning electron microscopy (SEM), and UV-visible spectroscopy. A Bruker-D2 powder diffractometer having Cu Kα radiation (with Ni filters) was used to test the crystalline quality, phase purity, and interplanar spacing of synthesized materials, with observations made in 2θ range of 20 to 80° for XRD. The morphology of synthesized samples was examined with scanning electron microscopy (JSM-5910, JEOL). A double-beam UV-visible spectrophotometer (T85+ pg Instruments) and an FTIR (Shimadzu) were utilized to find functional groups present in the synthesized materials. Quantitative phase analysis of the XRD data was performed using the MAUD (Materials Analysis Using Diffraction) software, (revision 2.99993, build 1147), employing the Rietveld refinement method.

2.4. Electrode preparation

Modified glassy carbon electrodes (GCEs) were prepared by drop-casting a slurry of nanoparticles mixed with ethanol and liquid Nafion binder onto a pre-cleaned electrode surface. For this purpose, the GCE was first polished using alumina slurry (MasterPrep polishing suspension 0.05 μm), followed by rinsing with deionized water. 2–3 μL of ethanol and 2–3 mg of electrocatalysts were mixed with 2–3 drops of 0.5% Nafion solution. A specific volume of about 5–6 μL of nanoparticles slurry was subsequently drop-casted onto the GCE and permitted to dry in an oven at 50 °C for 30 min. This modified electrode was employed for electrochemical study using a three-electrode configuration, deploying a platinum wire as counter electrode and an Ag/AgCl electrode as a reference.

2.5. Electrochemical characterizations and OER studies

Numerous electrochemical techniques were used to investigate the electrochemical characteristics of materials, including cyclic voltammetry (CV), linear sweep voltammetry (LSV), and square-wave voltammetry (SWV). Electrochemical measurements were evaluated by a Gamry 3000 ZRA potentiostat/galvanostat (USA) using a three-electrode configuration.

3. Results and discussion

3.1. X-ray diffraction

XRD analysis was conducted to explore structural and crystalline phases of studied NPs. The XRD analysis of C-NPs showed prominent peaks at 33°, 35.7°, 40.93°, 49.38°, 54.1°, 62.45°, and 64.1°, as shown in Fig. 1. These peaks correspond well with crystal structure of hematite (α-Fe_2O_3, JCPDS 01-073-2234 *via* search match method), particularly the (311) reflection at 35.7°, which is the most intense peak for this phase.[20] On the other hand, the XRD patterns of E-NPs and E-M-NPs show the presence of mixed phases of iron oxide consisting of primarily magnetite (Fe_3O_4) and/or maghemite (γ-Fe_2O_3) and small amount of an oxidized phase goethite (α-FeOOH).[20–22] It is difficult to differentiate between the peaks of maghemite and magnetite because most of their peaks occur at same 2θ and peak positions differ by very small amounts.[21] However, an exact match with JCPDS card was not achievable due to mixed phases (goethite, magnetite and maghemite) and doping. The small amount of goethite is indicated by a small peak at 20.4° (110) in all NPs synthesized using plant leaf extract.[22] The other peaks at 31.9° (220), 35.2° (311), 42° (400), 53.5° (422), and 57° (511) corresponds to magnetite as shown in Fig. 1.[20] Furthermore, the intensity of magnetite peak deviates from a usual XRD pattern where it should have high intensity. Such deviations are reported in literature and are attributed to the certain morphologies of NPs (due to synthesis methods) which may depress the

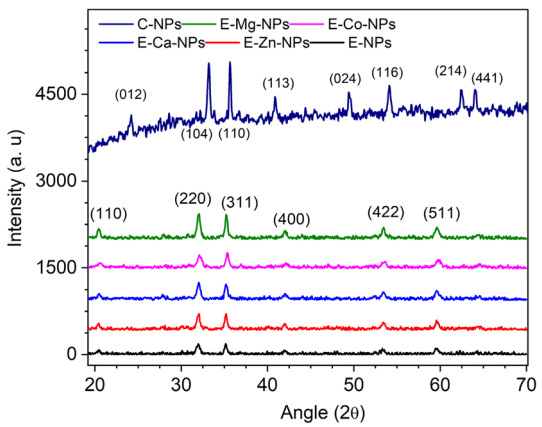

Fig. 1 XRD analysis of iron-oxide NPs and their doped NPs.

Table 1 The crystallite size, phase and *d*-spacing of NPs obtained through XRD analysis

Sr. no.	NPs	Crystallite size (nm)	Phase fraction (wt%)	*d*-spacing (nm)
1	E-NPs	19.33	Magnetite/maghemite = 98.38 ± 0.00	2.566
2	E-Zn-NPs	14.05	Goethite = 1.62 ± 26.90	2.549
3	E-Mg-NPs	16.84		2.549
4	E-Ca-NPs	16.92		2.549
5	E-Co-NPs	8.33		2.541
6	C-NPs	20.27	Hematite = 100 ± 0.00	2.516

intensity of certain peaks.[23] In order to investigate the weight percentages of each phase, quantitative phase analysis of E-NPs and E-M NPs was performed using Rietveld refinement, yielding 98.38 ± 0.00 wt% and 1.62 ± 26.90 wt% magnetite/maghemite and goethite, respectively. Because of the significant overlap of diffraction peaks arising from the similar spinel structures of magnetite and maghemite, their individual weight percentages could not be resolved.

This phase variation in the NPs synthesized from two different synthetic routes (with and without plant extract) is probably because the plant extract-based synthesis of NPs is influenced by the nature of the plant extract, which may lead to incomplete reduction of iron precursors, slower nucleation, and phase transformations favoring mixed phases.[24] Additionally, the capping by organic compounds in plant extracts can further hinder the formation of well-defined crystal structures. The E-M-NPs displayed slight shifting of peaks to higher angles, probably due to the tensile stress introduced because of interstitial doping of metals.[25]

The peak broadening in XRD can be used to determine the crystallite size using Scherer formula. The crystallite size provides the value of coherently diffracting domain size which may contain many particles and can be different from the particle size obtained through electron microscopy. A single particle may consist of multiple crystallites which means the particle size may be larger compared to the crystallite size calculated from Scherer equation.[26] On the other hand, the particle size obtained from SEM (discussed in forthcoming section) represents the physical and visually observable size of the particles as seen in microscopic images. The average crystallite sizes (D_{avg}) of all synthesized NPs, listed in Table 1, were evaluated *via* Scherrer equation (eqn (1)),[27]

$$D_{avg}(nm) = \frac{k\lambda}{\beta \cos \theta} \quad (1)$$

Here, D_{avg} is average crystallite size, K is the shape factor (0.9), λ is wavelength (0.154 nm), β is related to full-width half maxima (FWHM), while θ denotes peak position. The crystallite size of C-NPs was determined to be 20.27 nm, while for E-NPs, it was found to be in the range of 19.33 nm.[11,28] Among all NPs, E-Co-NPs exhibited the smallest crystallite size leading to significant variation in electrochemical properties relative to all other studied NPs. The *d*-spacing calculated from the 2θ peaks of 35.2° and 33° for extract-based NPs and C-NPs respectively, are also presented in Table 1.

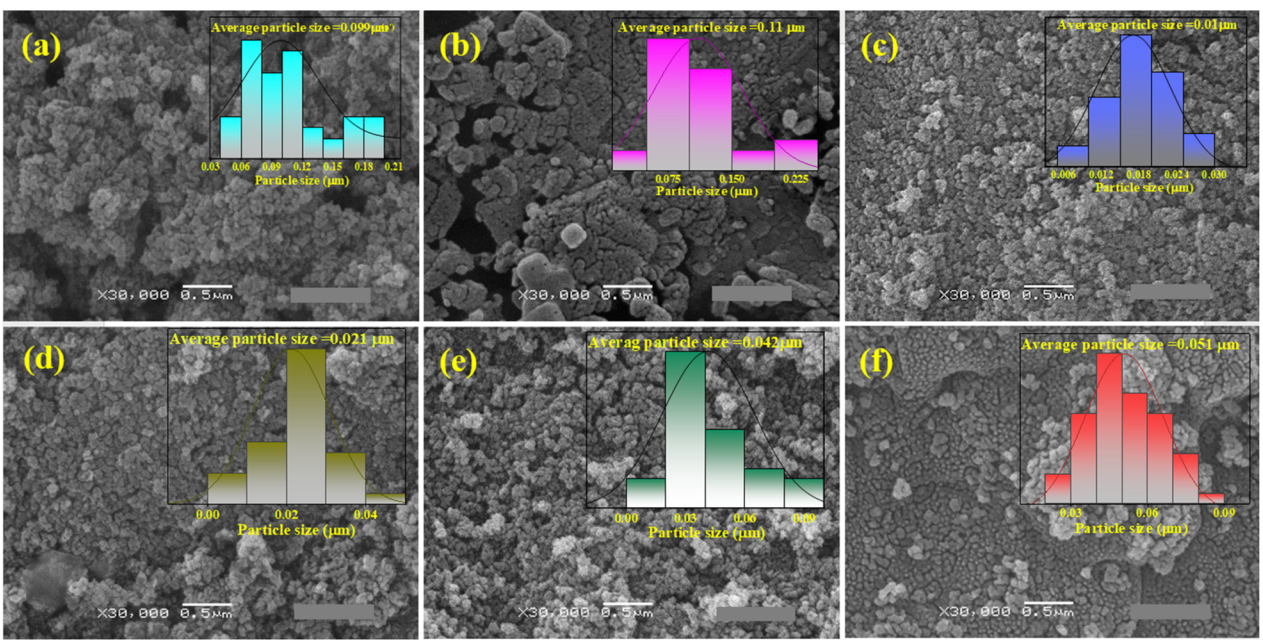

Fig. 2 SEM analysis of (a) E-NPs, (b) C-NPs, (c) E-Co-NPs, (d) E-Zn-NPs, (e) E-Mg-NPs, and (f) E-Ca-NPs.

3.2. SEM analysis

The SEM analysis of all synthesized NPs was executed to investigate their surface morphological characteristics. Fig. 2(a) shows the SEM image of E-NPs having agglomerated structure which generally leads to less easily available active sites; considerably decreasing the catalytic activity. However, C-NPs in Fig. 2(b), are composed of clusters of NPs that are uniformly dispersed. Fig. 2(c) depicts E-Co-NPs with a rough surface, indicating more adsorption of intermediates like OH* and OOH* during OER. In Fig. 2(d), E-Zn-NPs exhibit granular particles on a compact, porous sheet-like structure. Whereas, in E-Mg-NPs (Fig. 2(e)), morphology changes into a more open and irregular porous structure with Mg-doping, which improves charge transport and ions accessibility. In Fig. 2(f), E-Ca-NPs show a combination of smaller and larger particles that are not homogeneous in nature; and this inhomogeneity might lead towards lower catalytic efficiency. Particle size calculation of all synthesized NPs was done by taking twenty selected particles from each image and plotting particle size *versus* frequency as demonstrated in Fig. 2(a–f). The particle size appeared to be 0.09, 0.11, 0.01, 0.021, 0.042, and 0.051 μm for E-NPs, C-NPs, E-Co-NPs, E-Zn-NPs, E-Mg-NPs, E-Ca-NPs, respectively. The particle size obtained through SEM analysis is based on the image of the entire particle including agglomerates as it appear under the microscopy therefore it can be different from the crystallite size obtained through XRD.[26] As seen in the SEM micrographs, the agglomeration has resulted in larger particle size estimation compared to the crystallite size calculated from XRD analysis. Moreover, the highest particle size of C-NPs is consistent with the visual inspection of SEM micrographs where greater agglomeration can be seen.

The EDX analysis of all prepared NPs was done to confirm the doping of iron oxide NPs with Ca, Co, Zn, and Mg. The EDX spectra are shown in Fig. 3 along with the wt percentages of elements in the inset. EDX analysis confirmed the successful incorporation of dopant elements in iron oxide NPs. Importantly, the wt percentages of dopants obtained from EDX analysis often differ because all of the dopant amounts may not be incorporated in the crystal lattice due to difference in elemental size, limited solubility and segregation at the defects or surfaces leading to over or under estimation in EDX.[29] Moreover Cl^- ions can also compete with dopants or interfere in the doping process due to the use of metal chloride precursors ($FeCl_3$, $MgCl_2$, $CaCl_2$) during the NPs synthesis.[29]

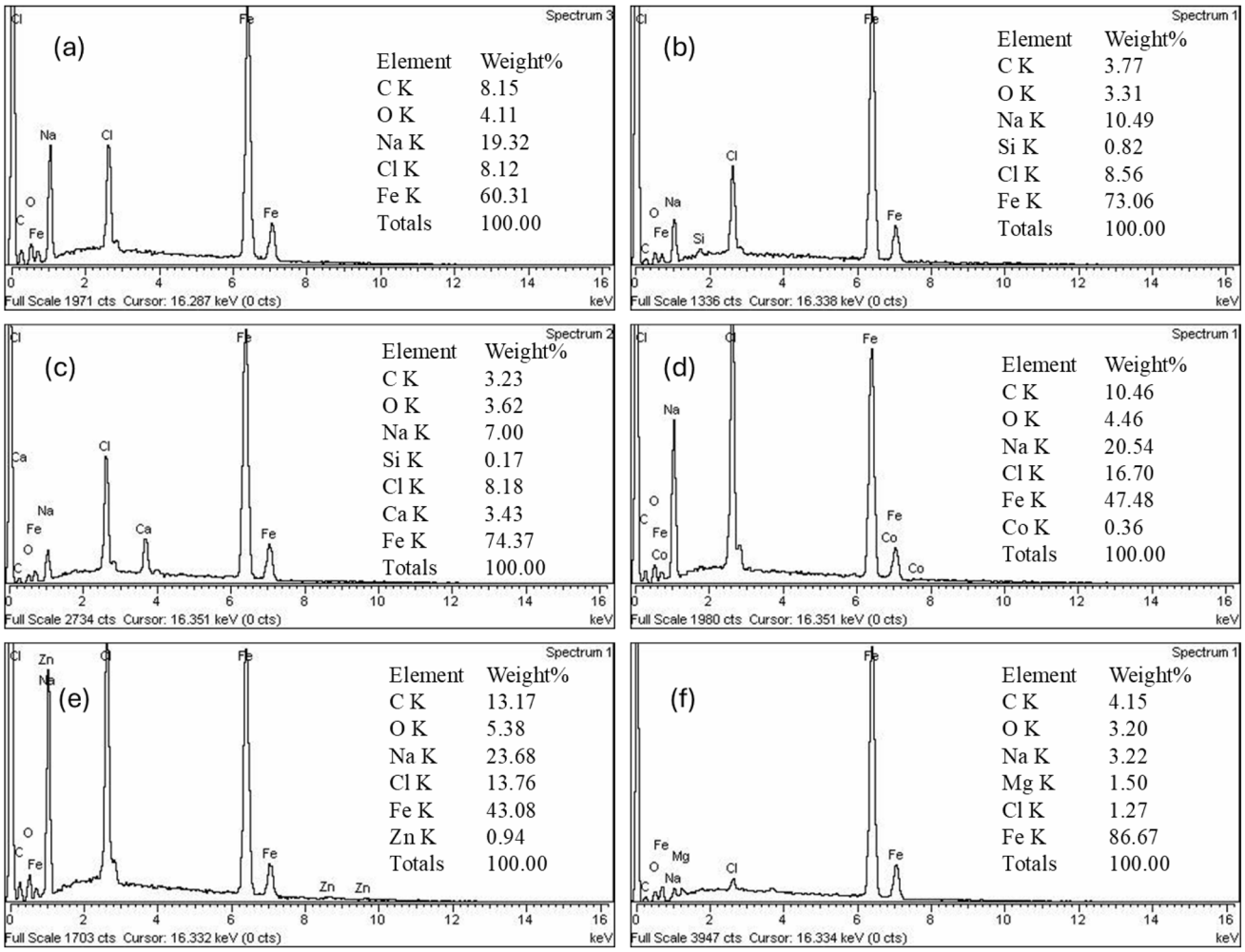

Fig. 3 EDX analysis; (a) E-NPs (b) C-NPs (c)E-Ca-NPs (d) E-Co-NPs (e) E-Zn-NPs (f) E-Mg-NPs.

3.3. Electronic absorption spectroscopy

The synthesized NPs were initially subjected to optical characterization using electronic absorption spectroscopy. The E-NPs exhibited two broad absorption peaks centered on 420 nm and 540 nm (ref. 30,31) (Fig. 4(a)).

The first peak at 420 nm is attributed to charge transfer transitions of Fe^{3+} ions. The second peak at 540 nm also appeared in C-NPs, suggesting that it is an intrinsic optical feature of the nanoparticles, possibly arising from Fe–O–Fe transitions or d–d transitions of Fe^{3+} ions.[31] The effect of 2% (w/w) dopant on the position of these peaks was further investigated. All doped samples depicted a blue shift by approximately 20 nm in the first peak compared to E-NPs while the peak at 540 nm remained unaffected in all NPs. Importantly, E-Co-NPs showed the most noticeable blue shift of all the doped NPs, with the first peak at 384 nm.

Direct and indirect Tauc plots (Fig. 4(b and c)) were deployed to calculate band gap of the all investigated NPs utilizing their electronic absorption spectra. Table 1 shows the band gap values that were determined from the Tauc plots. The band gap values (Table 2) were found to be ~2 eV with slight variation in the synthesised NPs,[28] except for Co-doped NPs exhibiting a modest decrease in band gap. Importantly, band gap of C-NPs was relatively higher to than that of E-NPs indicating that the plant extract-based synthesis method results in NPs with relatively lower band gap compared to the chemically synthesized ones.

3.4. Fourier transform infrared spectroscopy

FTIR spectra of iron oxide pristine and doped NPs synthesized by chemical and plant-extract routes were obtained to confirm the presence of specific functional groups. A broad and strong transmittance peak observed at 559 cm^{-1} is attributed to Fe–O stretching,[28] which confirmed the successful formation of iron oxide NPs. This peak typically appears in the range of 500–600 cm^{-1} for magnetite (Fe_3O_4), as well as maghemite (γ-Fe_2O_3) and is a signature of the metal–oxygen lattice vibrations in the spinel structure, as shown in Fig. 5. Its presence indicates that iron-oxide has been formed successfully *via* both routes, though crystallinity and exact phase may differ. The small peak at 857 cm^{-1} may corresponds to C–H out-of-plane bending vibrations or possibly Fe–OH bending, especially in cases where surface hydroxyl groups are present due to interaction with water or plant extract components.[32] A broad band at 1566 cm^{-1} is ascribed towards asymmetric stretching of carboxylate groups (COO^-) or C=C stretching vibrations of aromatic rings.[33] A peak observed around 2320 cm^{-1} is ascribed towards CO_2 that comes through atmosphere during synthesis.[34] In plant extract-based synthesis, this broad peak is prominent likely due to the presence of bio-organic compounds such as flavonoids, phenolic acids, or polyphenols that act as reducing and stabilizing agents.[35] These molecules contain functional groups like carboxylic acids and aromatic structures that bind to the NPs surfaces, preventing agglomeration and stabilizing the colloid. A broad hump present at 3476 cm^{-1} is associated with O–H stretching.[28] In plant extract-based NPs, this peak is broader and more intense due to hydrogen bonding between water molecules and plant-derived compounds containing hydroxyl groups. This band may also indicate the presence of phenolic –OH groups from plant extract.[28]

Table 2 Band gap of synthesized NPs calculated using direct and indirect Tauc plots

Sr. no.	NPs	Direct band gap (eV)	Indirect band gap (eV)
01	E-NPs	1.97	2.24
02	E-Zn-NPs	2.07	2.34
03	E-Mg-NPs	2.03	2.16
04	E-Ca-NPs	2.06	2.28
05	E-Co-NPs	1.98	2.00
06	C-NPs	2.01	2.03

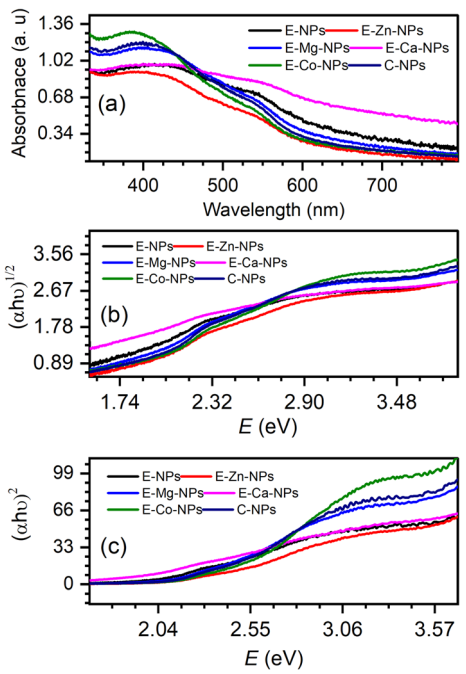

Fig. 4 (a) Electronic absorption spectra of all synthesized NPs (b) direct Tauc plot; (c) indirect Tauc plot for all NPs samples.

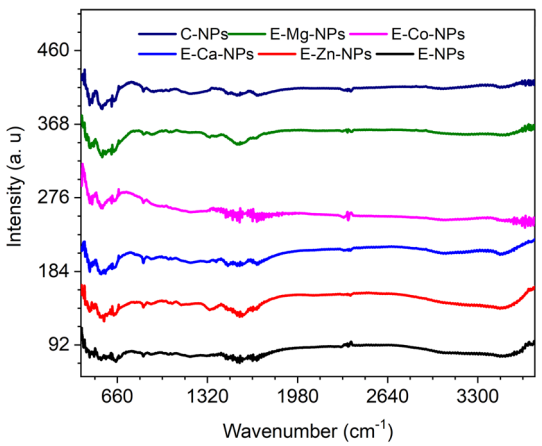

Fig. 5 FTIR analysis of the synthesized NPs.

3.5. Electrochemical analysis

Square wave voltammetry (SWV) is also used to electrochemically characterize the synthesized NPs. SWV was used to probe the redox behavior, oxidation state transitions and purity of NPs. The appearance of well-defined oxidation peaks associated with Fe(III) species confirms the successful formation of electrochemically active iron oxide phases, supporting the structural and compositional analysis obtained from XRD and other characterization techniques (Fig. 6). SWV of modified GCEs was performed in 1 M KOH solution having a potential window of −1.5 to 0.0 V. The electrochemical response of all electrodes is shown in Fig. 6. Two peaks at −0.9 V and −0.3 V were present in SWV of all synthesized NPs, indicating the reduction of Fe(III). The appearance of forward and reverse peaks in SWV indicated a quasi-reversible nature of the electrochemical process for all synthesized NPs. For reference, the I_f, I_b, and I_t of the E-Zn-NPs modified GCE is shown in the inset of Fig. 6, confirming quasi-reversible reaction.

According to literature, the peak at a less negative potential corresponds to the reduction of fresh Fe(III) ions, while the second peak at a more negative potential shows the reduction of "aged" Fe(III).[36] Aged Fe(III) is formed with time when Fe(III) aggregates, polymerizes, or restructures on the surface of the electrode. Moreover, C-NPs exhibited a higher peak current for the first cathodic peak compared to other synthesized NPs which indicate improved charge transfer or lower resistance at the modified GCE surface.[37] In addition, E-Zn-NPs modified GCE exhibited higher peak currents among the doped systems, along with a little shift towards lower potential, indicating enhanced charge transfer kinetics with better performance. The observed enhancement might be attributed to improved conductivity and a modified electronic structure due to the incorporation of Zn.[38]

3.6. OER studies

To investigate the onset potential (E_{onset}) for OER of synthesized NPs, electrochemical analysis was conducted using LSV to find as shown in Fig. 7(a). E-Co-NPs modified GCE had a much lower onset potential (0.937 V) than E-NPs (1.01 V) and C-NPs modified GCEs (1.03 V), indicating their excellent electrocatalytic potentials. The lower onset potential and higher current indicate more efficient oxygen evolution when using E-Co-NPs modified GCE. This fact can be attributed to extended surface roughness as depicted through SEM analysis (Fig. 2(c)). Fig. 7(b) shows CV cycles for E-Zn-NPs at GCE that were obtained through various scan rates in the range of 10 to 100 mV s^{-1} to get insights about electrode activity. The current density increases as the potential increases, which indicates better catalytic activity for water splitting. However, for effective water-splitting applications, these cycles need to be stable and reproducible, which means they need to last a long time while running continuously.

Effect of scan rate on current was also studied using LSV for all modified GCEs. Fig. 8(a) shows the effect of scan rate for E-Ca-NPs modified GCE where the current steadily increased by increasing the scan rate. As higher scan rates show efficient potential cycling at electrode surface; that ultimately results in

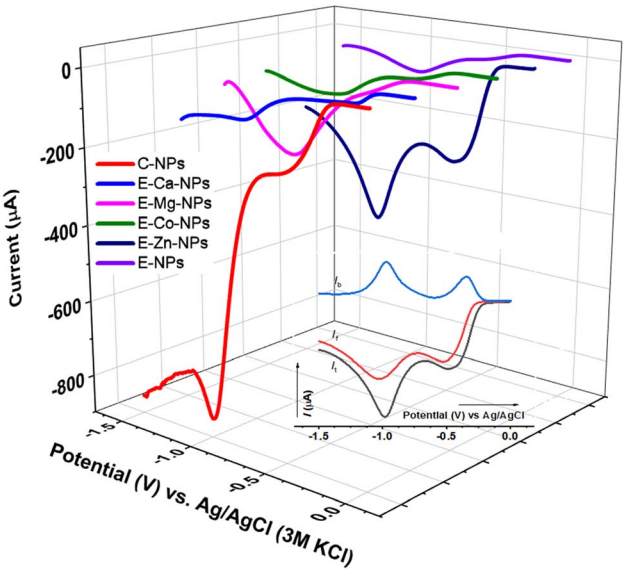

Fig. 6 SWV of modified GCEs in 1 M KOH at 5 mV s^{-1}. The inset shows the I_f, I_b, and I_t of the E-Zn-NPs modified GCE.

a better activity of the OER. The comparison of all electrodes shows a higher oxidation current of E-Co-NP modified GCE, demonstrating its better electrochemical activity at all scan rates (Fig. 8(b)). SEM analysis also supports the best electrochemical activity of E-Co-NPs by showing the smallest particle size, as depicted in Fig. 2(c). Smaller sized particles can lead to enhanced ECSA owing to more active sites; which essentially increase the electrochemical activity of the material. This is because more binding sites will be available for reaction intermediates (hydroxyl, oxo, and peroxo intermediates) formed during water oxidation.[39] The ECSA of all synthesized NPs was calculated through cyclic voltammetry (CV), as discussed in the

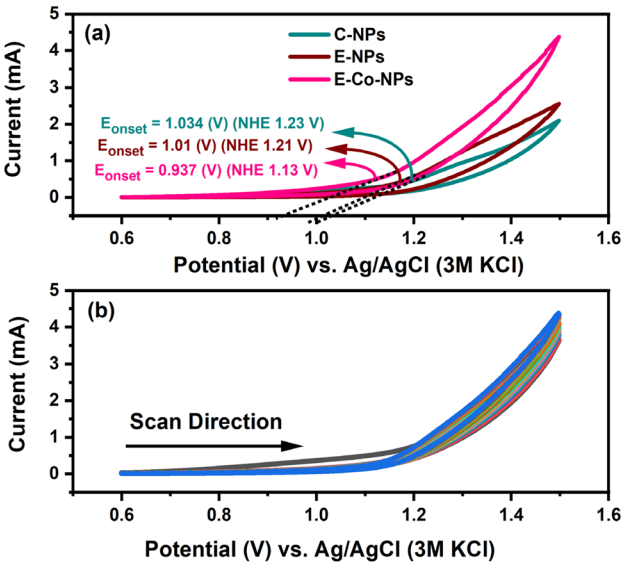

Fig. 7 (a) CVs of C-NPs, E-NPs, and E-Co-NPs modified GCEs at 100 mV s^{-1} (b) CV of E-Zn-NPs modified GCE at varying scan rate of 10–100 mV s^{-1}.

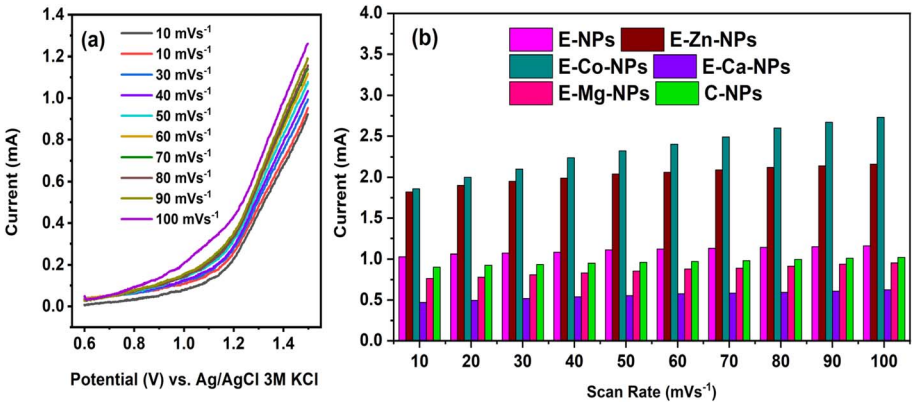

Fig. 8 (a) LSV of E-Ca-NPs modified GCE in 1 M KOH at varying scan rates of 10–100 mV s^{-1} (b) current *vs.* scan rate of all modified GCE measured using LSV.

forthcoming explanation, and confirmed the highest ECSA for E-Co-NPs, complementing LSV and SEM analysis.

OER was also studied through CV of all modified electrodes at different scan rates. CVs of E-Mg-NPs modified GCE at varied scan rates of 40–100 mV s^{-1} are shown in Fig. 9(a). From the results, it is evident that as the scan rate increases, the current response also increases linearly, similar to LSV. In Fig. 9(b), linear correlation among current and scan rate reveals the diffusion-controlled behaviour of the E-Mg-NPs at GCE, which correlates with adsorption efficiency of intermediates like OH^- or OOH that adhered to surface of electrode during the electrochemical reaction. The R^2 value of 0.99 further confirms the linearity of the Mg-doped NPs, that is a basic requirement for attaining the stability in OER. The CVs in the faradaic region (1.10–1.60 V) shows that electrochemical oxidation of water proceeds in this potential window. This potential range plays a significant role in electrochemical activity for water splitting; *via* providing higher current density with increased effectiveness of materials. The non-faradic area (0.60–1.0 V) is the region where preliminary no reaction takes place, and the current attained by the material is also negligible. The non-faradaic region can be employed to determine C_{dl}. CV data was utilized to calculate ECSA through eqn (2).[40]

$$\mathrm{ECSA} = \frac{C_{dl}}{C_s} \tag{2}$$

where C_s is the specific capacitance of the material whose values has been established for various metal electrodes in acidic and

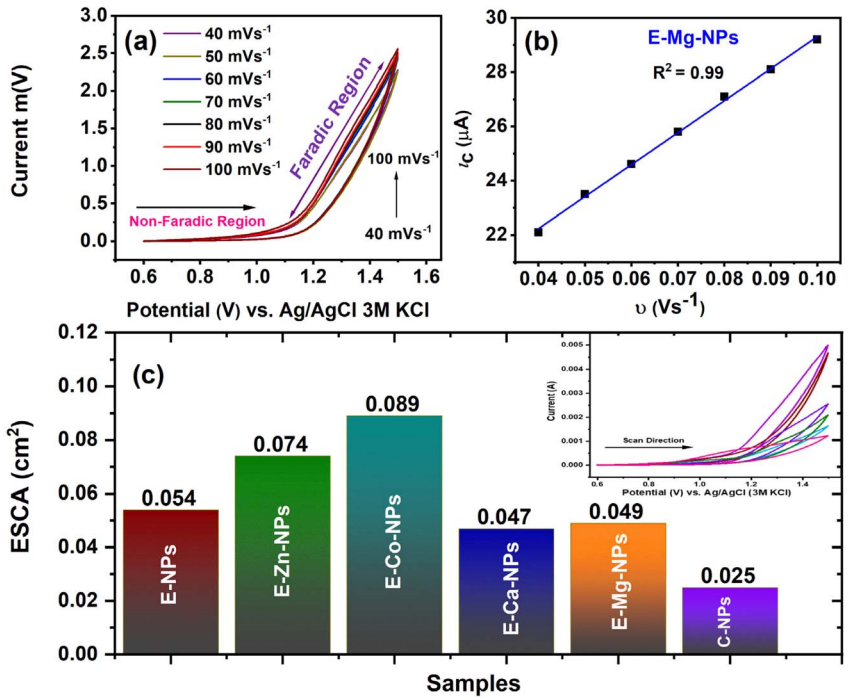

Fig. 9 (a) CVs of E-Mg-NPs modified GCE at different scan rates. (b) Randles–Sevick plot (c) bar graph representing ECSA of all electrocatalysts. The inset shows the comparative CV profiles of all electrocatalysts at 100 mV s^{-1}.

Table 3 The values of E_{onset}, ESCA, and current function slopes were obtained through LSV and CV of NPs

Sr. no.	NPs	E_{onset} *vs.* Ag/AgCl (v)	ECSA (cm^2)
1	E-NPs	1.011	0.04
2	E-Zn-NPs	0.960	0.60
3	**E-Co-NPs**	**0.937**	**0.70**
4	E-Ca-NPs	0.921	0.14
5	E-Mg-NPs	0.952	0.45
6	C-NPs	1.034	0.03

alkaline environments. The reported ranges of C_s in acidic medium may be from 0.015 to 0.110 mF cm^{-2} while in basic medium C_s may vary from 0.022 to 0.130 mF cm^{-2}. The value of 0.04 mF cm^{-2} for specific capacitance (C_s) is widely accepted as standard average value for metal oxides and hydroxides in alkaline medium.[41–44] It is important to note that C_s is not a universal constant and is strongly influenced by surface morphology, roughness, composition, porosity, crystallinity, and surface chemistry of the electrode material. Therefore, ECSA estimation based on double-layer capacitance (using an average C_s value), represents a limitation to determine the absolute ECSA values. However, this approach can be employed when direct experimental determination of C_s is not feasible, and it remains valid for relative comparison of ECSA among samples measured under identical experimental conditions. Importantly, all catalysts in this study were evaluated using the same assumed C_s value; therefore, the observed ECSA trends and performance comparisons remain internally consistent and meaningful.

The highest ECSA was found to be for E-Co-NPs aligning with the results of SEM and LSV. The enhanced electrochemical surface area of E-Co-NPs at GCE indicates a considerably more electrochemically accessible active sites, which improves the surface charge transfer, increases electrolyte accessibility, and promotes effective reactant adsorption. The increased surface roughness in the E-Co-NPs likely facilitates this significant increase in electrochemical surface area reflecting an improved electrocatalytic performance of E-Co-NPs. The calculated values of ECSA for all synthesised electrocatalysts are displayed in Fig. 9(c), along with an inset that indicates the comparative CV profiles of all electrocatalysts at 100 mV s^{-1}. The inset of Fig. 9(c) clearly shows that E-Co-NPs-GCE exhibits higher current response, in comparison to all other synthesized electrocatalysts.

Table 3 shows the values of E_{onset} and ECSA for all electrodes obtained through LSV and CV, respectively. All extract-based NPs (E-NPs and E-M-NPs) have lower E_{onset} and higher ESCA compared to C-NPs. This is also supported by XRD analysis which confirmed the less crystallinity in E-NPs/E-M-NPs compared to C-NPs. The better performance of the former indicates that plant extract-based synthesis approach of electrocatalysts has significantly contributed to the high potential for OER.

Fig. 10(a) depicts the plot of current *vs.* $\nu^{1/2}$, which was employed to determine the diffusion coefficient (D) of species at modified GCEs according to Randles–Sevcik equation (eqn (3)).[45]

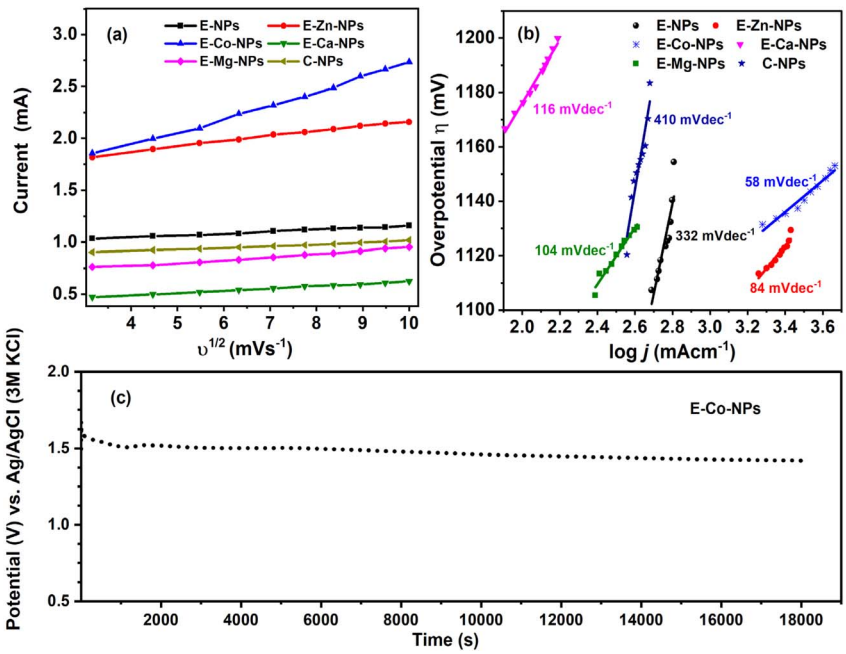

Fig. 10 (a) The plots of I *vs.* $\nu^{1/2}$ for all modified electrodes (b) plot of overpotential (η) *vs.* log j for all modified electrodes (c) chronopotentiometry curve on surface of E-Co-NPs at 10 mA cm^{-2} for 5 h.

Table 4 Kinetic parameters for OER at the electrode surfaces

Sr. no.	Samples	α	D (10^{-9} cm^2 s^{-1})	m_T (10^{-2} cm s^{-1})	TOF (s^{-1})	Tafel slope (mV dec^{-1})
1	E-NPs	0.072	0.18	0.06	0.25	332
2	E-Zn-NPs	0.071	1.23	1.56	0.35	84
3	**E-Co-NPs**	**0.071**	**8.55**	**4.20**	**0.38**	**58**
4	E-Ca-NPs	0.074	0.24	0.70	0.21	116
5	E-Mg-NPs	0.073	0.41	0.09	0.24	104
6	C-NPs	0.071	0.14	0.05	0.08	410

$$I = 2.99 \times 10^5 \; n\sqrt{(1-\alpha)n_\alpha}AC\sqrt{D}\sqrt{\nu} \quad (3)$$

where D denotes diffusion coefficient, n denotes number of electrons engaged in OER, α denotes transfer coefficient, A is considered as the glassy carbon electrode's area (0.07 cm^2), C denotes concentration of electrolyte, and ν is the scan rate in mV s^{-1}.

Value of α is between 0.1 and 0.7 and can be attained from eqn (4).

$$E - E_{1/2} = [0.048/(\alpha n_\alpha)] \quad (4)$$

where E is potential at which the current is measured and $E_{1/2}$ is peak potential at $I_{1/2}$.

The values of the transfer coefficient predict the nature of reaction; if $\alpha < 0.5$ the forward reaction is favored, if $\alpha > 0.5$ the reaction is favored in the reverse direction. The mass transport coefficient (m_T) is also obtained using eqn (5).[27]

$$m_T = [D/(RT/F\nu)]^{1/2} \quad (5)$$

The diffusion coefficient for E-Co-NPs modified GCE was found to be much higher compared to other electrodes. Hence, E-Co-NPs at GC electrode ameliorated the OER more effectively, as compared to other electrodes. The interaction of E-Co-NPs-GCE improved the electronic coupling and optimum energies of adsorption for reactive intermediates, which is crucial to an efficient OER.[46] The comparison of the plot of current *vs.* square root of scan rate for all electrodes is shown in Fig. 10(a) where the E-Co-NPs exhibited the best linear relationship with R^2 value of 0.99843 indicating a diffusion-controlled process.

Another important kinetic parameter that is generally used to evaluate activity of an electrocatalyst is turnover frequency (TOF). It tells about the intrinsic activity of electrocatalyst.

$$\text{TOF} = j \times A/4\times F \times n \quad (6)$$

Variables F, j, n, and A represent the Faraday constant, current density, moles of active catalyst, and electrode area, respectively,[47] enlisted in Table 4. E-Co-NPs modified GCE has attained significantly higher TOF as compared to other synthesized electrocatalysts, which validates the enhancement in its catalytic efficiency for OER. This enhancement was ascribed to the presence of Co^{2+}/Co^{3+} into the lattice of iron oxide which facilitates charge transfer capability, electronic conductivity, and modification in d-band center close to Fermi-level.[48,49]

The Tafel slopes were calculated from the plot of over-potential *vs.* log i to analyze the kinetics of catalytic activity for OER and electrocatalyst-support systems *via* eqn (7) and is shown in Fig. 10(b).

Table 5 Comparison of the performance metrics of different electrode materials for OER

Electrocatalyst	Synthesis mode	Medium	Tafel slope (mV dec^{-1})	TOF	Stability (h)	Ref.
RuO_2 (benchmark)	Chemically synthesized	1.0 M KOH	40–60	—	Poor	42
IrO_2 (benchmark)		1.0 M KOH	50–70	—	Good	42
α-Fe_2O_3 nanorings	Hydrothermal	1 M HCl	138	2.3	—	54
α-Fe_2O_3 (hematite)	Hydrothermal	1 M KOH	98	0.005	08	55
Co–Fe NPs	Green synthesized (*Seidlitzia rosmarinus)*	1 M KOH	63	—	—	56
Co_3O_4/α-Fe_2O_3	Co-precipitation	0.1 M KOH	62	—	—	50
Co:α-Fe_2O_3/γ-Fe_2O_3	ZIF-etching	1 M KOH	57	—	16	52
Co_3O_4–Fe_2O_3	Ball milling process	1 M KOH	144	—	100	49
Co_3Te_4–Fe_3C	Hydrothermal	1 M KOH	68	—	60	57
Zn/Fe–Co_3O_4	—	1.0 M KOH	54	—	120	58
ZnFeCo LDH	*In situ* growth	1 M KOH	59	—	28	59
$MgFe_2O_4$	Sol–gel	1 M KOH	317	—	Good	60
Mg–Fe_2O_4 (HESF)	Sol–gel	0.1 M KOH	97	—	—	61
E-NPs	Green synthesized	1 M KOH	332	0.25	—	This work
E-Zn-NPs	>do<	>do<	84	0.35	—	This work
E-Co-NPs	>do<	>do<	58	0.38	05	This work
E-Ca-NPs	>do<	>do<	116	0.21	—	This work
E-Mg-NPs	>do<	>do<	104	0.24	—	This work
C-NPs	Co-precipitation	>do<	410	0.08	—	This work

$$\eta = a + 2.303\frac{RT}{\alpha nF}\log j \quad (7)$$

where, η (mV) is over potential value calculated from potential value (E) of each sample, a is the intercept relative to the exchange current density (j_0), and j (**m**A cm s^{-1}) is current density, calculated according to geometrical area of electrode.

The Tafel slopes listed in Table 4 present the lowest Tafel slope for E-Co-NPs and highest for C-NPs which further support the higher OER activity of cobalt containing electrocatalysts *via* greater interaction of CoOOH with hydroxyl ions (OH^-) which is produced during oxygen evolution reaction.[50]

The long-term stability test on surface of best performer (E-Co-NPs) was studied *via* chronopotentiometry (CP) at current density of 10 mA cm^{-2} in 1 M KOH for 5 h (18 000 seconds). As depicted from Fig. 10(c), modified electrode based on E-Co-NPs exhibited stability with minimal fluctuation of potential throughout the period.

From Fig. 10(c), a gradual potential decay from 1.59 V to 1.51 V is observed within the first 1000 seconds which is a common reported behavior for transition metal oxide based OER electrocatalysts and is generally attributed to *in situ* surface reconstruction, electrochemical activation processes, and the formation of catalytically active hydroxide/oxyhydroxide species.[48,51,52] After the initial surface activation, gradual stabilization occurred with minimum potential drift. The potentials reached at 1.42 V after 5 h with total potential decay of $\Delta E =$ 170 mV for 5 h (0.567 mV min^{-1}). This behavior is dissimilar to RuO_2 which shows substantial activity degradation in basic medium.[53] No sudden failure or spikes were observed in potential throughout the measurement, confirming the excellent stability of electrocatalyst. The comparative study of all synthesized electrocatalysts with the reported electrocatalysts including standard benchmark ruthenium and iridium compounds employed for OER is given in Table 5. Green synthesized NPs present the comparable Tafel slopes in alkaline medium with E-Co-NPs attaining benchmark values (40–110 mV dec^{-1}).

4. Conclusion

The pursuit of a clean energy alternative to conventional fossil fuels in an environmentally friendly manner drives greater interest in hydrogen fuel. This study demonstrated the successful fabrication of pristine and doped iron oxide NPs using the leaf extract of *Ocimum tenuiflorum*. Zinc, magnesium, calcium, and cobalt were used as dopants. Diverse instrumental techniques including XRD, SEM, FTIR, and UV-visible spectroscopy for employed for characterization of NPs. SWV analysis verified the reversible nature of electrochemical reduction of all synthesized NPs where E-Zn-NPs depicted the best current response as compared to other doped electrocatalysts. OER studies revealed that E-Co-NPs modified GCE exhibited higher catalytic properties owing to high diffusion coefficients, mass transfer properties, greater ECSA, and lowest onset potential compared to pristine and other doped NPs. The turnover frequency (TOF) of these materials further confirmed their high electrochemical activity towards OER. The study showed that a plant extract-based synthesis approach produced more effective NPs with excellent OER potentials relative to chemically synthesized NPs.

Conflicts of interest

The authors declare no conflict of interest.

Data availability

The data supporting the findings of this study are available within the article. Additional raw data can be provided by the corresponding author upon reasonable request.

Acknowledgements

This work was supported and funded by the Deanship of Scientific Research at Imam Mohammad Ibn Saud Islamic University (IMSIU) (grant number IMSIU-DDRSP2602).

References

1 S. Hussain, N. Raza, I. Ijaz, A. Bukhari, Y. Xu, M. E. Salem and A. Shaheen, *Coord. Chem. Rev.*, 2025, **545**, 217023.
2 S. Ahmad, M. Khan, S. B. Khan and A. M. Asiri, *Inorg. Chem. Commun.*, 2024, **170**, 113421.
3 S. N. Hussain, N. Raza, T. S. Alomar, N. AlMasoud, H. Gul, G. Ashraf, M. Z. Ansari and G. Yasin, *Mater. Sci. Eng., B*, 2024, **302**, 117267.
4 L. Zhang, Y. Li, J. Peng and K. Peng, *Electrochim. Acta*, 2019, **318**, 762–769.
5 G. Liu, F. Xie, X. Cai and J. Ye, *ACS Catal.*, 2024, **14**, 8652–8665.
6 M. Nemiwal, T. C. Zhang and D. Kumar, *Int. J. Hydrogen Energy*, 2021, **46**, 21401–21418.
7 N. Arif, M. N. Zafar, M. Batool, M. Humayun, M. A. Iqbal, M. Younis, L. Li, K. Li and Y.-J. Zeng, *J. Mater. Chem. C*, 2024, **12**, 12653–12691.
8 Q. Chen, R. Wang, M. Yu, Y. Zeng, F. Lu, X. Kuang and X. Lu, *Electrochim. Acta*, 2017, **247**, 666–673.
9 J. Gautam, S. Y. Lee and S. J. Park, *Adv. Energy Mater.*, 2025, **15**, 2406047.
10 N. T. Tasnim, N. Ferdous, M. M. H. Rumon and M. S. Shakil, *ACS Omega*, 2023, **9**, 16–32.
11 A. Wahab, M. Imran, M. Ikram, M. Naz, M. Aqeel, A. Rafiq, H. Majeed and S. Ali, *Appl. Nanosci.*, 2019, **9**, 1823–1832.
12 N. Dogan, O. M. Dogan, M. Irfan, F. Ozel, A. Kamzin, V. Semenov and I. Buryanenko, *J. Magn. Magn. Mater.*, 2022, **561**, 169654.
13 G. Kasparis, A. P. Sangnier, L. Wang, C. Efstathiou, A. P. LaGrow, A. Sergides, C. Wilhelm and N. T. K. Thanh, *J. Mater. Chem. B*, 2023, **11**, 787–801.
14 S. Guo, H. Wang, W. Yang, H. Fida, L. You and K. Zhou, *Appl. Catal., B*, 2020, **262**, 118250.
15 J. S. Nyarige, A. T. Paradzah, T. P. Krüger and M. Diale, *Nanomaterials*, 2022, **12**, 366.

16 J. Talibawo, P. I. Kyesmen, M. C. Cyulinyana and M. Diale, *Nanomaterials*, 2022, **12**, 2961.
17 H. Yousaf, S. M. Muzaffar, S. Riaz, N. Ahmad, S. Shahzadi and S. Naseem, *J. Mater. Sci.: Mater. Electron.*, 2019, **30**, 4203–4218.
18 J. Prakash, A. A. Chaudhary, A. Somvanshi, B. Lal, Suman, M. Ramya, H. A. Rudayni, N. Raza, M. Fazil and T. Ahmad, *Sci. Rep.*, 2025, **15**, 30119.
19 G. I. Edo, A. N. Mafe, A. B. Ali, P. O. Akpoghelie, E. Yousif, E. F. Isoje, U. A. Igbuku, S. A. Ismael, A. E. A. Essaghah and D. S. Ahmed, *BioNanoScience*, 2025, **15**, 267.
20 H. Cui, Y. Liu and W. Ren, *Adv. Powder Technol.*, 2013, **24**, 93–97.
21 W. Kim, C.-Y. Suh, S.-W. Cho, K.-M. Roh, H. Kwon, K. Song and I.-J. Shon, *Talanta*, 2012, **94**, 348–352.
22 M. Kosmulski, E. Maczka, E. Jartych and J. B. Rosenholm, *Adv. Colloid Interface Sci.*, 2003, **103**, 57–76.
23 C. F. Holder and R. E. Schaak, *ACS Nano*, 2019, **13**, 7359–7365.
24 V. Akshay and M. Vasundhara, *Colloids Surf., A*, 2020, **603**, 125241.
25 S. Munir, S. M. Shah and H. Hussain, *Mater. Des.*, 2016, **92**, 64–72.
26 G. Kasi, N. Stalin, P. Rachtanapun, K. Jantanasakulwong, J. N. Halder, S. Phongthai, P. Worajittiphon, J. Seo and S. Thanakkasaranee, *Int. J. Mol. Sci.*, 2025, **26**, 4868.
27 M. Khan, N. K. Janjua, S. Khan, I. Qazi, S. Ali and T. Saad Algarni, *Coatings*, 2021, **11**, 257.
28 Atul, M. Kumar, A. Sharma, I. K. Maurya, A. Thakur and S. Kumar, *J. Taibah Univ. Sci.*, 2019, **13**, 280–285.
29 A. Roy, C. P. Healey, N. E. Larm, P. Ishtaweera, M. Roca and G. A. Baker, *ACS Nanosci. Au*, 2024, **4**, 176–193.
30 E. Fazio, M. Santoro, G. Lentini, D. Franco, S. P. P. Guglielmino and F. Neri, *Colloids Surf., A*, 2016, **490**, 98–103.
31 Y. He, Y. Miao, C. Li, S. Wang, L. Cao, S. Xie, G. Yang, B. Zou and C. Burda, *Phys. Rev. B:Condens. Matter Mater. Phys.*, 2005, **71**, 125411.
32 Q. Wen, W. Wei, Y. Li, D. Chen, J. Zhang, Z. Li and D.-a. Guo, *Sensors*, 2024, **25**, 50.
33 S. Anjum, R. Tufail, H. Saleem, R. Zia and S. Riaz, *J. Supercond. Novel Magn.*, 2017, **30**, 2291–2301.
34 F. Van Broekhuizen, I. Groot, H. Fraser, E. F. van Dishoeck and S. Schlemmer, *Astron. Astrophys.*, 2006, **451**, 723–731.
35 H. H. Shwe and S. Win, *IEEE-SEM*, 2019, **7**, 84–90.
36 M. Taillefert, A. Bono and G. Luther, *Environ. Sci. Technol.*, 2000, **34**, 2169–2177.
37 F. Aslam, A. Shah, N. Ullah and S. Munir, *ACS Appl. Nano Mater.*, 2023, **6**, 6172–6185.
38 Suman, S. Chahal, A. Kumar and P. Kumar, *crystals*, 2020, **10**, 273.
39 P. Wang, S. Zhang, Z. Wang, Y. Mo, X. Luo, F. Yang, M. Lv, Z. Li and X. Liu, *J. Mater. Chem. A*, 2023, **11**, 5476–5494.
40 M. Khan, N. K. Janjua, A. Ahmad, R. Luque, A. A. Al-Kahtani and A. M. Tighezza, *Int. J. Energy Res.*, 2022, **46**, 14161–14173.
41 S. Jung, C. C. McCrory, I. M. Ferrer, J. C. Peters and T. F. Jaramillo, *J. Mater. Chem. A*, 2016, **4**, 3068–3076.
42 C. C. McCrory, S. Jung, I. M. Ferrer, S. M. Chatman, J. C. Peters and T. F. Jaramillo, *J. Am. Chem. Soc.*, 2015, **137**, 4347–4357.
43 C. C. McCrory, S. Jung, J. C. Peters and T. F. Jaramillo, *J. Am. Chem. Soc.*, 2013, **135**, 16977–16987.
44 S. Watzele, P. Hauenstein, Y. Liang, S. Xue, J. Fichtner, B. Garlyyev, D. Scieszka, F. Claudel, F. Maillard and A. S. Bandarenka, *ACS Catal.*, 2019, **9**, 9222–9230.
45 S. Khan, I. Arshad, S. Aftab, J. Arshad, M. Khan, S. S. Shah, N. K. Janjua, M. Mohany, Y. Ning and H. Li, *ChemistrySelect*, 2024, **9**, e202402784.
46 A. S. Joseph, S. Vasudevan and U. G. Panicker, *Mater. Sci. Semicond. Process.*, 2025, **200**, 109984.
47 U. De Silva, J. Masud, N. Zhang, Y. Hong, W. P. Liyanage, M. A. Zaeem and M. Nath, *J. Mater. Chem. A*, 2018, **6**, 7608–7622.
48 M. S. Burke, M. G. Kast, L. Trotochaud, A. M. Smith and S. W. Boettcher, *J. Am. Chem. Soc.*, 2015, **137**, 3638–3648.
49 S. Heo, C. Kim, J. Lee, S. Jin, J. Y. Jeong, S. W. Myeong, H. Lee, E. j. Park, M. Park and S. M. Choi, *J. Am. Ceram. Soc.*, 2025, e20633.
50 K.-L. Ng, K.-Y. Kok and B.-H. Ong, *ACS Appl. Nano Mater.*, 2017, **1**, 401–409.
51 M. W. Louie and A. T. Bell, *J. Am. Chem. Soc.*, 2013, **135**, 12329–12337.
52 J. P. G. D. S. Soares, A. D. A. Lourenço, R. A. Raimundo, M. A. Morales Torres, R. B. da Silva, A. L. Menezes de Oliveira, D. A. Macedo and F. F. da Silva, *ACS Appl. Nano Mater.*, 2025, **8**, 11655–11668.
53 S. Cherevko, S. Geiger, O. Kasian, N. Kulyk, J.-P. Grote, A. Savan, B. R. Shrestha, S. Merzlikin, B. Breitbach and A. Ludwig, *Catal. Today*, 2016, **262**, 170–180.
54 X. Liang, J. Qian, Y. Liu, Z. Zhang and D. Gao, *RSC Adv.*, 2020, **10**, 29077–29081.
55 B. Ahmmad, K. Leonard, M. S. Islam, J. Kurawaki, M. Muruganandham, T. Ohkubo and Y. Kuroda, *Adv. Powder Technol.*, 2013, **24**, 160–167.
56 F. Gheybi, M. Rashidi-Huyeh and M. R. Mohammadi, *Discover Mater.*, 2025, **5**, 132.
57 M. Abdul, M. Zhang, T. Ma, N. H. Alotaibi, S. Mohammad and Y.-S. Luo, *Nanoscale Adv.*, 2025, **7**, 433–447.
58 Q. Chen, Y. Huang, W. Duan, Q. Su, Y. Wang, F. Bao, J. Zhang and W. Guo, *Mater. Horiz.*, 2025, **12**, 9780–9788.
59 J. Han, J. Zhang, T. Wang, Q. Xiong, W. Wang, L. Cao and B. Dong, *ACS Sustain. Chem. Eng.*, 2019, **7**, 13105–13114.
60 S. Maitra, R. Mitra and T. Nath, *Curr. Appl. Phys.*, 2021, **27**, 73–88.
61 T. Erdil, C. Ozgur, U. Geyikci, E. Lokcu and C. Toparli, *ACS Appl. Energy Mater.*, 2024, **7**, 7775–7786.